Heterojunction interface engineering enabling high onset potential in Sb2Se3/CdS photocathodes for efficient solar hydrogen production

G. Liang, T. Liu, M. Ishaq, Z. Chen, R. Tang, Z. Zheng, Z. Su, P. Fan, Xianghua Zhang, S. Chen

Heterojunction interface engineering enabling high onset potential in Sb_2Se_3/CdS photocathodes for efficient solar hydrogen production

*Guangxing Liang[a], Tianxiang Liu[a], Muhammad Ishaq[a], Zejia Chen[a], Rong Tang[a], Zhuanghao Zheng[a], Zhenghua Su[a], Ping Fan[a], Xianghua Zhang[b], Shuo Chen[a,]**

[a]Shenzhen Key Laboratory of Advanced Thin Films and Applications, Key Laboratory of Optoelectronic Devices and Systems of Ministry of Education and Guangdong Province, College of Physics and Optoelectronic Engineering, College of Materials Science and Engineering, Shenzhen University, Shenzhen, 518060, China

[b]Univ Rennes, CNRS, ISCR (Institut des Sciences Chimiques de Rennes) UMR 6226, F-35000 Rennes, France

[*]Corresponding author: Email: chensh@szu.edu.cn (S. Chen)

ABSTRACT

Sb_2Se_3 has emerged as an ideal photocathode candidate profiting from its superior optoelectronic properties, and has gained rapid development in photocurrent generation. However, achieving both high photocurrent density (J_{ph}) and onset potential (V_{on}) is of immense importance. In this work, self-assembled growth of Sb_2Se_3 with large crystal grains, benign orientation, and accurate composition was first fulfilled via a combination reaction involving sputtered and selenized Sb precursor. Then Mo/Sb_2Se_3/CdS/Pt photocathodes were constructed. In addition to the selenization condition-dependent Sb_2Se_3 film quality that influenced device performance, an additional Sb_2Se_3/CdS heterojunction post-annealing has demonstrated a strong positive effect. Thanks to the band alignment modification, charge transport strengthening, and surface wettability improvement, the champion device delivered J_{ph} of 16.25 mA cm^{-2}, V_{on} of 0.52 V_{RHE}, and HC-STH conversion efficiency of 2.58%. Such an interface engineering can pave the way for fabricating high V_{on} Sb_2Se_3 photocathode to broaden its scope of solar hydrogen production applications.

Keywords: Sb_2Se_3; Photocathode; Interface engineering; Onset potential; Solar hydrogen production

1. Introduction

Due to the shortage of fossil fuels and deterioration of environmental condition, exploring renewable and environmental-friendly energy resources has become inevitable for a carbon-neutral and sustainable society. In recent years, solar energy and hydrogen energy, regarded as carbon-free and clean energy, have attracted tremendous research attentions [1]. Moreover, combining the advantages of those two energy forms, and achieving efficient solar-to-hydrogen (STH) seems more interest, especially for practical application scenarios. STH can be accomplished from water splitting via processes of photocatalysis, photovoltaic-electrochemical and photoelectrochemical [2]. Among them, the photoelectrochemical (PEC) process is a promising technique, involving a cell system that simultaneously function as a light harvester to absorb solar energy, and an electrolyser to perform chemical reactions to produce H_2 [3]. To achieve a high STH conversion efficiency, the light absorbing photoelectrode materials should be capable of absorbing sufficient sunlight, transporting to the electrolyte efficiently, and remaining long-term stable without photocorrosion [4]. To date, numerous semiconductors have been developed for PEC solar hydrogen production, such as Si [5], SiC [6], Cu_2O [7], CdTe [8], Cu-chalcogenides [9-12] and Sb-chalcogenides [13,14]. However, the continuous exploration of earth-abundant and low-cost candidates are still getting growing concerns.

Antimony selenide (Sb_2Se_3) has remarkable material advantages and superior optoelectronic properties when used in PEC processed solar hydrogen production. Sb_2Se_3 is a simple V-VI binary semiconductor with only one stable crystalline phase,

the constitutes of Sb and Se also show low-toxicity, low-cost, and earth-abundant nature. Sb_2Se_3 possesses a proper bandgap of 1.0-1.2 eV, high absorption coefficient (>10^5 cm^{-1}), decent carrier mobility (~10 cm^2 V^{-1}), and long carrier lifetime (~60 ns) [15-17]. As a PEC photocathode, the theoretical maximum photocurrent density (J_{ph}) of Sb_2Se_3 can approach to 40.9 mA cm^{-2} under AM 1.5G solar light illumination with 100% photon-to-current conversion, which is comparable to those well-known utilizers of Si and Cu(In,Ga)Se_2 [18-20]. Furthermore, Sb_2Se_3 has absolute internal stability in some commonly used neutral or acidic electrolytes, no obvious self-reduction or photocorrosion phenomena can be observed [21]. As Sb_2Se_3 has an intrinsic one-dimensional (1D) crystal structure accumulated by $[Sb_4Se_6]_n$ nanoribbons with van der Waals forces along the [100] and [010] axes, strong covalent bonds along [001] axis, it tends to grow with 1D morphology [22]. For instance, Moon *et al.* used various Sb-Se molecular inks to grow 1D nanoneedle, nanowire, nanorod, and hierarchical nanorod structured Sb_2Se_3 photocathodes via spin coating method [23-26]. However, it has also been reported that compact film-type Sb_2Se_3 with favorable [hk1] preferential orientation enables higher carrier transportability and less boundary recombination loss, which can achieve much superior PEC performance compared with that of 1D nanostructured counterpart [27]. To date, only a few studies associated with thermal evaporation, close-spaced sublimation, and magnetron sputtering processed Sb_2Se_3 film photocathodes have been reported [18,27,28]. Compared with the extensive Sb_2Se_3 film deposition techniques for photovoltaic applications, the controllable preparation of Sb_2Se_3 photocathodes still needs further investigation.

Since the first Sb_2Se_3 photocathode for PEC water splitting reported by Moon *et al.* in 2017 [23], extensive research has been focused on this interesting scenario. Various architectures and engineering efforts (e.g., absorber engineering, interfaces engineering,

co-catalyst engineering, and tandem engineering) are continuously emerging [27,29-31]. Within a very short period of time, Sb_2Se_3-based photocathodes achieved a rapid development in terms of J_{ph} from 2 mA cm^{-2} to 35 mA cm^{-2}, a record half-cell STH (HC-STH) conversion efficiency of 4.7% based on FTO/Au/Sb_2Se_3/AL/PABA/TiO_2/Pt configuration, and a record unbiased STH efficiency exceeding 10% via Sb_2Se_3 photocathode coupled with semitransparent perovskite photovoltaic [14,23,32]. Accordingly, the J_{ph} has reached 80% of its thermodynamic limit. Thus, in order to further improve the PEC performance of Sb_2Se_3 photocathode, future research should be focused on maximizing the J_{ph} while producing sufficiently large photovoltage (i.e., onset potential, V_{on}). A high V_{on} is essential to compensate the unavoidable potential losses induced by charge transport within the photoelectrodes and/or the overpotentials at the electrode/electrolyte interface. Some experimental surface/interface engineering, such as decorating polycrystalline Sb_2Se_3 thin films at surface by conjugated molecules to passivate the surface defects, inserting n-type CdS buffer layer at the Sb_2Se_3/TiO_2 interface to reduce valence band mismatch, have been conducted as attempts to improve the V_{on} of Sb_2Se_3 photocathodes [14,28]. Despite such endeavors, the further optimization of V_{on} and STH efficiency via a simple and effective strategy also needs further exploration.

In this work, Sb_2Se_3 light absorbing films with large crystal grains, benign orientation, and stoichiometric composition have been prepared via an effective combination reaction involved with pre-sputtered and post-selenized Sb metallic precursors. After sequential deposition of CdS buffer layer, and Pt co-catalyst, an efficient thin film photocathode with configuration of Glass/Mo/Sb_2Se_3/CdS/Pt was fabricated. Interestingly, a mediate temperature post-annealing of Sb_2Se_3/CdS heterojunction has been found to remarkably enhance the V_{on} and PEC performance. A champion

photocathode can deliver a J_{ph} of 16.25 mA cm^{-2} at 0 V versus a reversible hydrogen electrode (RHE, V_{RHE}), an interesting V_{on} of 0.52 V_{RHE}, and a HC-STH conversion efficiency of 2.58%. Our results provide a simple and bright avenue toward high V_{on} Sb_2Se_3 photocathode for PEC processed solar hydrogen production.

2. Experimental section

2.1. Preparation of Sb_2Se_3 thin films

Soda lime glass was chosen as substrate, which need to be ultrasonically cleaned in sequential detergent, acetone, isopropanol, and ethanol solution for 10 min, respectively. Before Sb_2Se_3 thin film deposition, Mo as back contact layer was deposited first using DC magnetron sputtering based on a dense Mo target. A double-pressure sputtering of Mo (~ 1 um thickness) was applied with a first 1.5 Pa of 15 min to improve adhesion, and then 0.5 Pa of 60 min to ensure compactness. Meanwhile, high-purity argon gas (>99.999%) was introduced at a flow rate of 40 sccm, and the sputtering power was fixed at 30 W. In Subsequent, Sb precursor thin film was deposited using RF magnetron sputtering, with argon flux of 40 sccm, a fixed power of 35 W, and a relatively low deposition pressure of 0.5 Pa. To obtain crystalline Sb_2Se_3 thin films, an effective post-selenization heat treatment of Sb precursor was implemented to induce *in-situ* combination reaction and self-assembled growth. In detail, the Sb film and high-purity Se powder (99.999%) were separately placed into a double-chamber vacuum tubular furnace. A working pressure of 5×10^4 Pa was maintained to provide sufficient Se partial pressure during the selenization. The Se powder side temperature was kept at 400 °C, while the Sb precursor side temperatures were ramped up to different setting values of 360 °C, 380 °C, 400 °C, 420 °C, and 440 °C, respectively. After a dwelling process, the Sb_2Se_3 thin films were naturally cooled down to room temperature.

2.2. Preparation of Sb_2Se_3 photocathode

After the deposition of Sb_2Se_3 thin films, CdS buffer layer was deposited upside via chemical bath deposition (CBD) process. The deionized water, $CdSO_4$ aqueous solution (0.015 M), thiourea aqueous solution (0.75 M), and ammonium hydroxide aqueous solution were sequentially added into a specific container with attached Glass/Mo/Sb_2Se_3 pieces. The container was then placed in a 80°C water bath under consecutive stirring for 9 min. Afterwards, the samples were rinsed with deionized water and dried in an oven. Importantly, an additional post-annealing treatment of Sb_2Se_3/CdS heterojunction interface was performed at 280 °C for 5 min using rapid thermal process (RTP) under argon atmosphere. Pt as co-catalyst was sputtered on the top side by using a 108 Auto Sputter Coater under an applied current of 20 mA for 50 s. Finally, Mo substrate was exposed at the corner, and low-temperature (60 °C) solidified Ag colloids were painted onto this fresh surface to form metallic contact. Overall, Fig. 1 represents a schematic illustration of the preparation process of Sb_2Se_3 thin film photocathode with configuration of Glass/Mo/Sb_2Se_3/CdS/Pt.

2.3. Characterizations

The crystal structure of the as-prepared films was measured by X-ray diffraction (XRD, Ultima-iv) with CuK_α radiation under operation conditions of 40 kV and 40 mA. The scanning electron microscope (SEM, SUPRA 55) was utilized to observe the surface and cross-sectional morphologies of the films, and an energy dispersive spectroscope (EDS, BRUKER QUANTAX 200) coupled with the SEM was used to analyze the corresponding chemical compositions. Transmission electron microscope (TEM) characterizations were performed by using a FEI Titan Cubed Themis G2 300 microscope. The sample was prepared by ablating the film device using focused ion

beam (FIB, FEI Scios). The surface morphologies and roughness of the films were examined using atomic force microscope (AFM) conducted by NT-MDT Spectrum Instruments under the semi-contact mode. The surface states were also analyzed via X-ray photoelectron spectroscopy (XPS, ESCALAB 250Xi). Contact angles were measured on a contact angle meter (PERFECT WAM-100) at room temperature. A Lambda 950 UV-Vis-NIR spectrophotometer was used to investigate the optical properties of the Sb_2Se_3 films, the bonding information were further characterized through Raman spectroscopy (Renishaw, InVia). Capacitance-voltage (*C–V*) measurements were applied at an AC amplitude of 30 mV and a frequency of 50 kHz under dark condition at room temperature. The DC bias voltage during the *C–V* measurements was applied from -0.5 V to 0.15 V.

2.4. PEC measurements

PEC performance was measured by using a CHI660e electrochemical workstation with a conventional three-electrode configuration. Ag/AgCl in saturated KCl was used as the reference electrode, Pt-wire as the counter electrode, and the Sb_2Se_3 photocathode as the working electrode. It was performed under 100 mW cm^{-2} AM 1.5G simulated sunlight illumination in 0.5 M H_2SO_4 electrolyte. The measured potential ($V_{Ag/AgCl}$) can be converted to V_{RHE} by employing the following Nernst equation [23]:

$$V_{RHE} = V_{Ag/AgCl} + 0.059 \times PH + 0.198 \quad (1)$$

HC-STH conversion efficiency (corresponds to the real applied bias photon-to-current efficiency (ABPE)) was calculated according to the following equation [27]:

$$HC - STH\ (\%) = J_{ph} \times \left(V_{RHE} - V_{H^+/H_2}\right)/P_{SUN} \times 100\% \quad (2)$$

where V_{RHE} is the potential of the working electrode against the electrolyte with respect to RHE, J_{ph} is the photocurrent density obtained under the applied bias of V_{RHE}, V_{H^+/H_2}

is 0 V_{RHE}, and P_{SUN} is 100 mW cm^{-2}.

The PEC impedance spectroscopy (PEIS) was obtained under light illumination with frequencies ranging from 0.1 Hz to 100 KHz at 0 V_{RHE}. Mott-Schottky (*M-S*) measurement was carried out to verify the flatband potential (E_{fb}) of the Sb_2Se_3 thin film, which was conducted in dark, scanned from 0.2 to 0.5 V_{RHE} with a V_{rms} of 0.01 V, and at frequency of 1 kHz. The E_{fb} was determined from the equation [33]:

$$\frac{1}{C_{sc}^2} = -\frac{2}{(\varepsilon_0 \varepsilon_{sc} A^2 e N_A)}(E_{apl} - E_{fb} - \frac{k_B T}{e}) \quad (3)$$

where C_{sc} is the capacitance of the semiconductor spatial charge region, ε_0 is the permittivity in vacuum, ε_{sc} is the dielectric constant (i.e., 15 for Sb_2Se_3 [34]), A is the active area, e is the elemental charge, N_A is the density of acceptors, E_{apl} is the applied potential, k_B is the Boltzmann constant, and T is the absolute temperature. The measured potential (vs. standard hydrogen electrode (SHE)) can be converted to absolute energy (vs. vacuum) by employing the equation [35]:

$$Energy\ (vs.\ vacuum) = -eE_{apl}\ (vs.\ SHE) - 4.44\ eV \quad (4)$$

3. Results and discussion

3.1. Characterization of Sb_2Se_3 thin films

A low-cost Mo conductive film was sputtered first on the glass substrate to replace the conventional back contact layer of Au. It shows a prominent (110) crystallographic plane belonging to cubic phase of Mo, a smooth surface, and compact quasi-vertical growth crystals, according to the XRD pattern and SEM images (Fig. S1, Supporting Information). Afterwards, an effective combination reaction involved with sputtered and selenized Sb precursors was used to prepare high-quality Sb_2Se_3 light absorbing thin films. The XRD pattern of Sb precursor film reveals that all the diffraction peaks match well with the JCPDS standard card (No. 35-0732) of the hexagonal phase of

metallic Sb (Fig. S1, Supporting Information). Surface and cross-sectional SEM images also demonstrate a non-compact morphology consisted of small grains, and a thickness of approximately 350 nm. The acquired uniform Sb films were subjected to selenization heat treatment at different temperatures and durations to obtain series of Sb_2Se_3 thin films. Fig. 2a shows the XRD patterns of the Sb_2Se_3 obtained at selenization temperatures of 360 °C, 380 °C, 400 °C, 420 °C, and 440 °C. All of the specimens are in good agreement with orthorhombic Sb_2Se_3 (JCPDS Card No. 15-0861, pbnm space group) without any detectable impurities or secondary phase. An obvious increase of peak intensities with increasing the temperature from 360 °C to 380 °C suggests an onset crystallization of the Sb_2Se_3 thin films upon heat treatment. Moreover, three major diffraction peaks of (211), (221), and (002) show sharp characteristics, indicating highly crystalline nature, also with a preferential growth orientation of [hk1]. Such perpendicular growth of the Sb_2Se_3 grains is highly beneficial to promote the charge carriers transport throughout absorber layer, and reduce the recombination loss at grain boundaries and interfaces [36]. The top-view SEM images, and the corresponding EDS determined Sb/Se elemental ratios of the Sb_2Se_3 thin films are also presented in Fig. 2b-f. At a selenization temperature of 360 °C, the film was composed of tiny grains, a slightly higher Sb/Se ratio of 0.69 was referring to a partial crystallization. For the thin films selenized at 380 °C and 400 °C, a more compact and uniform coverage of the surface can be observed, accompanied by a synchronous increase of the average grain size from approximately 380 nm to 830 nm. The detailed temperature-dependent frequency histograms versus Sb_2Se_3 grain size distribution are depicted in Fig. S2 (Supporting Information). Notably, the thin film selenized at 400 °C has a Sb/Se ratio (0.67) that is quite close to the standard stoichiometric ratio (2/3) for Sb_2Se_3. Further improving the temperature led to emerge pinholes on the surface (Fig. 2e), and then

caused a serious decomposition with distinct micro-voids at a high temperature of 440 °C (Fig. 2f), which can be attributed to Se re-evaporation from Sb_2Se_3 under its high vapor pressure, as confirmed by the EDS results. A parallel selenization duration-dependent structure and morphology evolution also demonstrated a similar crystal growth, and an optimal selenization of 15 min (Fig. S3, Supporting Information). Therefore, it's crucial to control the selenization scenario to obtain high-quality Sb_2Se_3 thin film with high crystallinity, benign orientation, large grain size, and accurate chemical composition.

Raman spectra of the Sb_2Se_3 thin films exhibit two major peaks located at 190 and 210 cm^{-1} (Fig. 3a). The dominant peak at 190 cm^{-1} could be ascribed to the Sb-Se vibration in the Sb_2Se_3 pyramidal symmetrical unit, while the secondary peak at 210 cm^{-1} was ascribed to heteropolar Sb-Se stretching vibration in Se chains [37]. The absence of other observable characteristic peaks belonging to secondary phase and/or oxidation of Sb further confirmed the high purity of the as-prepared Sb_2Se_3 thin films. To further investigate its optical properties, the reflection spectra were obtained via UV/Vis/NIR spectrophotometer by using glass as substrate and covering a range from 300 nm to 1500 nm. The reflection spectra showed a similar short wavelength cut-off edge of approximately 1000 nm for Sb_2Se_3 films. The slight variation can be attributed to the difference in grain size and surface roughness of the thin films. The important information of bandgap (E_g) was further calculated according to the following formulas.

$$2\alpha d = ln\left[\frac{R_{max} - R_{min}}{R - R_{min}}\right] \quad (5)$$

$$\alpha hv = C(hv - E_g)^n \quad (6)$$

where α is the absorption coefficient, d is thickness, the reflectance falls from R_{max} to R_{min} due to the intrinsic absorption of light by the sample [38]. The latter is a typical Tauc formula, where C is a constant, h is the Planck's constant, v is the photon

frequency, and n is an index defined by 0.5 for direct and 2.0 for indirect bandgap semiconductor. The thin films exhibited a similar direct bandgap of approximately 1.22 eV under different selenization heat treatment, as described in Fig. 3c. The calculated E_g values agree well with that given in literature for crystalline Sb_2Se_3 thin film [39]. Moreover, such an ideal low-bandgap also permits an interesting broad sunlight harvesting, making Sb_2Se_3 an attractive candidate as PEC photocathode for solar hydrogen production.

3.2. PEC performance of Sb_2Se_3-based photocathodes

Fig. 4 shows the PEC performance of the Sb_2Se_3-based photocathodes by using the classical 3-electrode PEC measurements. A schematic illustration of this process is presented in Fig. 4a. The as-fabricated Sb_2Se_3 photocathode showed obvious layer structure with configuration of Glass/Mo/Sb_2Se_3/CdS/Pt (Fig. 4b). Sb_2Se_3 thin film consisted of large columnar grains was quasi-vertically grown on the substrate, and was uniformly covered by CdS buffer layer. Both the interfaces of Mo/Sb_2Se_3 and Sb_2Se_3/CdS showed characteristics of void-free and smooth contact, which was beneficial to suppress the possible interfacial recombination loss. Moreover, the obtained Sb_2Se_3 photocathode was homogeneous in appearance with an area over 4 cm^2 (inset in Fig. 4b), implying great potential in large-area application scenarios. Fig. 4c shows an experimental observed photograph with obvious hydrogen bubbles emerged from Sb_2Se_3 photocathode surface to the acidic electrolyte of 0.5 M H_2SO_4 (pH 0) under AM 1.5G simulated sunlight illumination. The chopped light determined current density-potential (*J-V*) curves of the pristine Sb_2Se_3, Sb_2Se_3/Pt, and Sb_2Se_3/CdS/Pt photocathodes are shown in Fig. 4d. Obviously, the pristine Sb_2Se_3 photocathode lacked significant PEC photoresponse with a very low cathodic J_{ph}. After loading Pt co-catalyst, a slight improvement in J_{ph} (~4 mA cm^{-2}, at 0 V_{RHE}) was achieved. With

the further insertion of an n-type CdS buffer layer between Sb_2Se_3 and Pt, remarkable improvement in photocurrent and photovoltage can be observed, suggesting an efficient separation and transfer of the photo-generated electron-hole pairs, and therefore induced electrochemical reactions at the electrode/electrolyte interface. In addition, with increasing the selenization temperature of Sb_2Se_3 thin films from 360 °C to 400 °C, a synchronous increase of J_{ph} can be observed (Fig. 4e). It was closely related to a much superior absorber layer quality with higher crystallinity, larger grain size, and more accurate chemical composition. The prominent [hk1] growth orientation of Sb_2Se_3 also enabled higher carrier transport and less recombination loss, thus improving the PEC performance. As a result, the champion photocathode selenized at 400 °C could achieve an interesting J_{ph} of 16.25 mA cm^{-2} at 0 V_{RHE}. Fig. 4f shows the linear swept *J-V* curves of the Sb_2Se_3/CdS/Pt photocathodes under dark and continuous simulated sunlight illumination, presenting similar variation upon the selnization temperature. Moreover, another important indicator of V_{on}, typically defined as the potential at which the steep *J-V* curves begins, herein, was precisely determined by extrapolating the *J-V* curves at the rapidly increasing region (Fig. S4, Supporting Information). Accordingly, a first positively shifted V_{on} values from 0.36 V_{RHE} to 0.52 V_{RHE}, and then decreased to 0.44 V_{RHE}, both matched well with the J_{ph} variations, implying completely efficient contribution to Hydrogen Evolution Reaction (HER). Then the corresponding HC-STH conversion efficiencies were calculated (according to Equation (2)) to direct diagnose the efficiencies for PEC photoelectrodes with three-electrode configuration, assuming 100% of the Faradaic efficiency and negligible overpotential of the counter reaction [14,40]. As shown in Fig. 4g, the maximum HC-STH values for the representative 360 °C, 380 °C, 400 °C, and 420 °C selenized devices were 0.89% (at 0.18 V_{RHE}), 1.73% (at 0.22 V_{RHE}), 2.58% (at 0.26 V_{RHE}), and 2.10% (at 0.22 V_{RHE}), respectively. Thus, an

appropriate selenization of Sb_2Se_3 is important for not only the photocurrent, but also the photovoltage and fill factor. It is worth mention that a maximum V_{on} of 0.52 V_{RHE} represents one of the highest values for Sb_2Se_3 photocathodes. Especially, it is comparable to those devices with structure complicated CdS/TiO_2 double buffer layer, or Sb_2Se_3 thin films with solution processed surface restoration by conjugated molecules [14,28]. Table 1 summarizes the key parameters of our Sb_2Se_3 thin film photocathode, compared to most of the reported Sb_2Se_3-based photocathodes [18,24,26-28,41,42]. By contrast, the PEC performance of our device is comparable to those state-of-the-art devices, especially with a higher V_{on}.

Fig. 5a-c displays the current density-time (*J-T*) curves of the representative 380 °C, 400 °C, and 420 °C selenized Sb_2Se_3 photocathodes under AM 1.5G simulated sunlight illumination at 0 V_{RHE}. As shown in Fig. 5a, when the light was on, the J_{ph} rapidly increased form 0 mA cm^{-2} to 12.53 mA cm^{-2}, and then sharply returned to its initial value as the light was turned off. This light response remained the same after over 110 cycles, indicating the excellent reversibility and stability of this Sb_2Se_3 PEC photocathode. A similar photoresponse can be seen for other two photocathodes, presenting approximately J_{ph} of 16 mA cm^{-2} and 14 mA cm^{-2}, respectively, also consistent with their *J-V* measurement results. Importantly, the champion device maintained ~87% of its initial J_{ph} of 16 mA cm^{-2} after operation for 60 min (Fig. 5d), suggesting long-term stability, and is comparable to those reported Sb_2Se_3 photocathodes with additional TiO_2 or C_{60} as protection layer [26,31]. According to literature, the as-deposited CdS buffer layer may exhibit partial photocorrosion due to the accumulation of injected charge to a point where the redox of CdS becomes thermodynamically favorable [43]. However, herein, no obvious degradation in stability can be observed for $Mo/Sb_2Se_3/CdS/Pt$ and $Mo/Sb_2Se_3/CdS/TiO_2/Pt$ photocathodes

(Fig. S5, Supporting Information). It was possibly benefit from the additional Sb_2Se_3/CdS heterojunction post-annealing, which could improve the crystallinity and stability of CdS to some extent, and also promote the charge separation and transfer to kinetically suppress the photocorrosion of CdS, resulting in a qualified long-term stability of our device in absence of other protection layer. Afterwards, to further understand the intrinsic stability (i.e., life span) of the light absorbing material, a photocorrosion stress test was implemented for the bare Sb_2Se_3 thin film via cyclic voltammetry (Fig. 5e). The absence of significant photocorrosion currents or redox peaks after 200 cycles strongly confirmed the remarkable tolerance of Sb_2Se_3 for practical PEC processed solar hydrogen production.

3.3. Effects of heterojunction interface engineering on device performance

To emphatically analyze the origin of a high V_{on} in this work, the important Sb_2Se_3/CdS heterojunction post-annealing should be first scrutinized. As mentioned in device preparation section, an additional interface engineering of Sb_2Se_3/CdS heterojunction post-annealing was performed with RTP process (Fig. 1d). It was designed according to the reported positive effects on Sb_2Se_3 solar cells with heterojunction heat treatment to induce elemental inter-diffusion, and energy-level alignment modification, therefore enhanced the open-circuit voltage and power-conversion efficiency [44]. Thus, for the sake of comparison, *J-V* curves of the optimized Sb_2Se_3/CdS photocathodes (with post-annealing, denoted as W annealing), and the counterpart (without post-annealing, denoted as W/O annealing) are presented in Fig. 6a and b. Obviously, compared to the non-annealed photocathode with J_{ph} of 6.18 mA cm^{-2}, the annealed photocathode (Sb_2Se_3/CdS (W)) showed a significant enhancement of J_{ph} to 16.25 mA cm^{-2} (at 0 V_{RHE}), indicating more effective carrier generation and less recombination loss. Likewise, the annealed device also exhibited higher HC-STH conversion efficiency at

more positive potential, and an over two times increase of V_{on} from 0.27 V_{RHE} to 0.52 V_{RHE} (Fig. 6c, and Fig. S4 (Supporting Information)). More insights of the impact of Sb_2Se_3/CdS heterojunction post-annealing on the band alignment were proposed and analyzed. As shown in Fig. S6 (Supporting Information), the *M-S* plot has a negative slop, indicating the inherent p-type semiconductor characteristic of the as-prepared Sb_2Se_3 thin film. The obtained E_{fb} of 0.65 V_{RHE} was approximately considered as the valence band potential (E_V) [45], and then the conduction band potential (E_C) can be calculated combined with its optical bandgap (E_g of 1.225 eV). Fig. 6d shows the $1/C^2$–V curves of the photocathodes based on *C-V* measurements, from which the heterojunction-dependent built-in voltage (V_{bi}) values can be determined. After linear fitting and extrapolating to x-axis, the yielded V_{bi} values were 0.29 V and 0.51 V for the non-annealed and annealed Sb_2Se_3/CdS heterojunction, respectively. Thus, the energy band diagram was illustrated in Fig. 6e, the SHE values of Sb_2Se_3 were converted to an absolute energy scale according to Equation (4) (see Experimental section), while the data regarding CdS energy levels was obtained from the reference [46]. For Sb_2Se_3/CdS (W/O) heterojunction, a little conduction band offset (CBO) would permit transfer of photo-generated electrons from bulk electrode to electrode-electrolyte interface for hydrogen evolution with assistance of Pt co-catalyst. Meanwhile, the large valence band offset (VBO) might create an energy barrier that prevent the transfer of photo-generated holes toward the electrode-electrolyte interface for recombination [47]. However, a quite small V_{bi} (0.29 V) would directly restrict the V_{on} of PEC photocathode. Then for the Sb_2Se_3/CdS (W) heterojunction, as shown in Fig. 6e, a schematic of the post-annealing induced Cd and S atoms diffused into Sb_2Se_3 absorber layer was illustrated according to our hypothesis (more evidences will be given later). The valence electrons of Cd are less than that of Sb, thus replacing Sb with Cd (i.e., Cd_{Sb} antisite) constitutes P-type

doping, the increased shallow acceptor density can lead to a down-shifting of its quasi-Fermi level position, and therefore enlarge V_{bi} according to the following equation [48]:

$$V_{bi} = \frac{k_B T}{q} \ln\left(\frac{N_A N_D}{n_i^2}\right) \quad (7)$$

where k_B is the Boltzmann constant, T is the temperature, q is the elementary charge, n_i is the intrinsic carrier concentration, N_A and N_D are the acceptor density and donor density in the Sb_2Se_3 layer and CdS buffer layer, respectively. Overall, such substantial improvement of V_{bi} (0.51 V) could promote the separation of photo-generated electron-hole pairs, which was undoubtedly beneficial for the highly interesting J_{ph}, V_{on} and PEC performance for the annealed Sb_2Se_3/CdS (W) photocathode.

In addition to the energy-level alignment modification, the charge transport kinetics influenced by such interesting interface engineering was also in-depth investigated. The transient photocurrent decay spectra of the non-annealed Mo/Sb_2Se_3/CdS (W/O)/Pt and annealed Mo/Sb_2Se_3/CdS (W)/Pt photocathodes were measured and shown in Fig. 7a. Both devices showed a "spike-like" transit when under sudden illumination, indicating the existence of carrier recombination effect. However, the annealed photocathode possesses a smaller photocurrent spike as compared to the non-annealed counterpart, demonstrating attenuated charge recombination and enhanced carrier transfer, and it was closely related to the Sb_2Se_3/CdS interface engineering. Meanwhile, the charge transfer efficiency (η_{tran}) was also calculated, which was defined as the ratio of the instantaneous photocurrent density (J_{inst}) and the steady-state photocurrent density (J_{ss}) [49]. The obtained η_{tran} of 70% for the annealed photocathode was significantly higher than that of the non-annealed counterpart with η_{tran} of 34%. Furthermore, the charge separation efficiency (η_{sep}) was also estimated from AM 1.5G solar spectrum (Fig. S7b, Supporting Information) and light harvesting efficiency (*LHE*, Fig. 7b), which can be calculated based on the following equations [25,50]:

$$J_{ph} = J_{abs} \times \eta_{sep} \times \eta_{tran} \quad (8)$$

$$LHE = 1 - 10^{-A(\lambda)} \quad (9)$$

$$J_{abs} = \int_{300}^{\lambda_e} \frac{\lambda}{1240} \times N_{ph}(\lambda) \times LHE(\lambda) d\lambda \quad (10)$$

where J_{ph} represents the measured photocurrent density, J_{abs} is the photocurrent density calculated by assuming 100% conversion of the absorbed photons to current density, λ_e is the absorption edge wavelength of the photocathode, N_{ph} (λ) is the photon flux (mW m^{-2} nm^{-1}), A (λ) is the absorbance at wavelength λ (see Fig. S7a, Supporting Information). The calculated η_{sep} values also showed a positive shift from 49% to 63% after heterojunction treatment.

PEIS measurements were then performed on the non-annealed and annealed photocathodes, respectively. Fig. 7c shows the Nyquist plots, a graph with double arcs was emerged for the non-annealed photocathode, while only a single arc can be observed for the annealed counterpart. Similarly, the former bode diagram consisted of two regions, one at high frequencies (~15 kHz), and the other at low frequencies (~200 Hz) (Fig. 7d). However, the latter bode plot exhibited only one region with a peak frequency of 3 KHz. Equivalent circuit was then employed for fitting the PEIS data, as shown in Fig. 7e and f. For the non-annealed photocathode, the equivalent circuit model consisted of one series resistance (R_s) and two parallel pairs of resistor-capacitor (R-C) components. To be specific, R_s represents the series resistance at Mo/Sb_2Se_3 back-contact interface. R_1 and C_1 (high frequency arc derivate) represent the charge transport resistance between Sb_2Se_3/CdS interface, and the corresponding capacitance within the semiconductor heterojunction and depletion region. While, R_2 and C_2 can be ascribed to the charge transfer/reaction resistance and surface-state capacitance of the Helmholtz layer at the electrode-electrolyte interface, respectively [42,51]. Interestingly, as shown in Fig. 7f, the pair of resistance R_1 and capacitance C_1 was disappeared when fitting the

results of the annealed device, implying the absence of recombination, further confirming a more efficient photo-generated charge carriers' separation and transport inside the photoelectrode after an additional Sb_2Se_3/CdS heterojunction post-annealing. Meanwhile, compared to that of non-annealed photocathode, the smaller R_2 value (26.7 Ω) of the annealed photocathode indicated its quicker photoelectrons transfer kinetics, and more efficient HER reactions occurred at electrode-electrolyte interface. A schematic (Fig. 7e and f) illustration of the photo-generated electron-hole pairs, recombination at interface, behaviors of electron's drifting and hole's drifting are also clearly presented. Finally, the corresponding calculated values associated to charge transport kinetics parameters are summarized in Table 2. The reduced recombination and the promotion of charge separation/transfer/reaction enabling the overall improvement of PEC performance for the annealed photocathode.

3.4. Morphological and structural analysis of the Mo/Sb_2Se_3/CdS/Pt photocathodes

TEM analysis was performed to further characterize the morphological and structural characteristics of the Mo/Sb_2Se_3/CdS/Pt photocathodes. As shown in Fig. 8, the representative cross-sectional TEM image of the annealed device displays an obvious layered structure with approximate thickness of 800 nm, and 70 nm for Sb_2Se_3, and CdS layers, respectively. A thin $MoSe_2$ interfacial layer (~30 nm) can also be observed between Mo conductive layer and Sb_2Se_3 absorber layer, which was reasonable to occur via combination reaction of Mo and Se during the selenization process. It has been reported that such an interfacial layer with appropriate thickness could improve the carrier transport and reduce the recombination loss, consistent with an acceptable R_s value (4.6 Ω) in PEIS results [52]. According to the high-resolution TEM (HRTEM) images taken at Sb_2Se_3/CdS interface (Fig. 8b), it displayed compact, well-adherent, and pinhole-free characteristics, which was really beneficial for reducing charge carrier

recombination and current leakage. The absence of lattice distortion or amorphous layer further validated a high-quality Sb_2Se_3/CdS heterojunction upon post-annealing. A lattice fringe with 0.321 nm interplanar d-spacing can be assigned to (111) plane of CdS. The Gaussian blur processed high-angle annular dark field scanning transmission electron microscope (HAADF-STEM) image (Fig. 8d) obtained at the bulk region of the Sb_2Se_3 thin film clearly revealed its 1D crystal structure with $(Sb_4Se_6)_n$ nanoribbons stacked in parallel in the [001] direction. Fig. 8e presents an atomic resolution HAADF-STEM image taken at the region near the Sb_2Se_3/CdS interface, i.e., the red rectangle area in Fig. 8b. It is known that the contrast of atomic columns in the image is approximately proportional to the mean square atomic number (Z^2) of the constituent atoms [53]. Thus, combined with the atomic crystal structure of Sb_2Se_3 viewed along [001] direction (Fig. 8g), the "bright dots" with strong intensity can be assigned to the Sb-dominated atomic columns (Z_{Sb} of 51), while the "dark dots" with much lower intensity matched well with Se-occupied atomic columns (Z_{Se} of 34). Fig. 8f shows the intensity profile of a row of atoms as marked by the red rectangle in Fig. 8e. Notably, an abnormal peak with lower intensity was observed at the original Sb-dominated site, implying a localized cation substitution by an element with a Z number between 34 and 51. In this case, it was highly likely to be Cd (i.e., Cd_{Sb}), which has been highlighted as blue sphere in the assumed position. Both the EDS elemental line scans and the TEM-coupled EDS elemental mapping results (Fig. 8h and i) clearly demonstrated a uniform distribution of Sb and Se within the bulk Sb_2Se_3 absorber layer, while an inter-diffusion of Cd and S into Sb_2Se_3 layer occurred at the heterojunction interface. Such interesting atomic diffusion and substitution can be verifiably ascribed to the additional heterojunction post-annealing, especially compared to the results of the non-annealed device (Fig. S8, Supporting Information).

3.5. Surface wettability and states analysis

Finally, the wettability of the pure Sb_2Se_3, Sb_2Se_3/CdS (W/O annealing), and Sb_2Se_3/CdS (W annealing) films were investigated, which could directly affect the electrochemical reactions occurred at electrode-electrolyte interface. An important indicator of contact angle (*CA*) was determined by the surface characteristics of solid (e.g., roughness of solid surface, free energy of solid surface) and liquid (e.g., surface tension of liquid) [54]. As shown in Fig. 9a-c, *CAs* of pure Sb_2Se_3 and Sb_2Se_3/CdS (W/O annealing) films were derived to 44.31° and 45.36°, respectively. While the value of Sb_2Se_3/CdS (W annealing) dramatically dwindle to 19.28°, suggesting an obvious improvement of wettability after heterojunction post-annealing. The increased wettability could provide more exposed reaction sites, facilitate photoelectrons transfer from photoelectrode to electrolyte to induce HER reactions, and therefore improved PEC performance. To provide more insight into the impact of heterojunction post-annealing on the surface wettability, AFM measurements were conducted to check the morphologies and surface roughness of the corresponding thin films. As shown in Fig. 9d-f, after depositing CdS buffer layer, more clearly crystal grain profiles can be observed, especially with a minimum value of root-mean-square (RMS) surface roughness for Sb_2Se_3/CdS (W/O annealing) film. However, according to the roughness-dependent wettability model proposed by Wenzel, the roughness will make a naturally hydrophilic surface (*CA*<90°) more hydrophilic [55]. Then in this case, Sb_2Se_3/CdS (W annealing) film with a higher RMS roughness value would improve its wettability, which has been corroborated by the *CA* measurement results. In addition, XPS measurements were further carried out to check the surface states of the Sb_2Se_3/CdS (W/O annealing) and Sb_2Se_3/CdS (W annealing) films. As shown in Fig. S9 (Supporting Information), no obvious peak shift of both Cd-3d and S-2p XPS spectra

can be observed, a slight decrease of the relative peak intensity further confirmed the Cd and S atoms diffused into Sb_2Se_3 absorber layer after heterojunction post-annealing. Overall, such surface modification really demonstrated an efficient RTP processed Sb_2Se_3/CdS heterojunction interface engineering, and therefore to achieve high performance photocathode.

4. Conclusion

In summary, Sb_2Se_3 light absorbing films were successfully prepared via an effective combination reaction involving sputtered and selenized Sb precursor films. Self-assembled growth of Sb_2Se_3 with micron-sized crystal grains, [hk1] preferential orientation, standard stoichiometric composition, and suitable bandgap (~1.2 eV) can be fulfilled under an optimized selenization scenario. Sb_2Se_3 photocathodes with configuration of Mo/Sb_2Se_3/CdS/Pt were constructed, and the corresponding PEC performance were systematically investigated. The selenization condition-dependent device performance concluded an optimal temperature of 400 °C with duration of 15 min. In addition, an interesting interface engineering of Sb_2Se_3/CdS heterojunction post-annealing has been found to significantly contribute to the device performance. Compared to the non-annealed counterpart, J_{ph} increased from 6.18 mA cm^{-2} to 16.25 mA cm^{-2} at 0 V_{RHE}, V_{on} increased from 0.27 V_{RHE} to 0.52 V_{RHE}, HC-STH conversion efficiency synchronously increased from 0.39% to 2.65%. The champion efficiency is comparable to the state-of-the-art Sb_2Se_3-based photocathodes, V_{on} of 0.52 V_{RHE} also represents one of the highest values so far. It has demonstrated that heterojunction post-annealing could induce Cd and S inter-diffusion to modify the energy-level alignment, reduce the recombination of photo-generated carriers at the heterojunction interface, enhance the charge separation and transfer within the photoelectrode, and improve the surface wettability at the electrode/electrolyte interface, therefore enhance the overall

PEC performance. This study clearly provides a simple interface treatment strategy to effectively optimize both J_{ph} and V_{on} of Sb_2Se_3 photocathode, making it an attractive candidate for highly efficient PEC processed solar hydrogen production applications.

Declaration of Competing Interest

The authors declare that they have no known competing financial interests or personal relationships that could have appeared to influence the work reported in this paper.

Acknowledgments

This work was supported by National Natural Science Foundation of China (No. 62074102, 62104156), Guangdong Basic and Applied Basic Research Foundation (2020A1515010805) China, Key Project of Department of Education of Guangdong Province (No. 2018KZDXM059) China, Science and Technology plan project of Shenzhen (20200812000347001, JCYJ20190808153409238) China. The authors wish to acknowledge the assistance on (TEM/STEM/FIB) received from the Electron Microscope Center of the Shenzhen University.

Appendix A. Supplementary data

Supplementary data related to this article are provided.

References

[1] X. Li, L. Zhao, J. Yu, X. Liu, X. Zhang, H. Liu, W. Zhou, Water Splitting: From Electrode to Green Energy System, Nano-Micro Lett. 12(1) (2020) 131. https://doi.org/10.1007/s40820-020-00469-3.

[2] J.H. Kim, D. Hansora, P. Sharma, J.W. Jang, J.S. Lee, Toward practical solar hydrogen production-an artificial photosynthetic leaf-to-farm challenge, Chem. Soc. Rev. 48(7) (2019) 1908-1971. https://doi.org/10.1039/c8cs00699g.

[3] K. Sivula, R. van de Krol, Semiconducting materials for photoelectrochemical energy conversion, Nat. Rev. Mater. 1(2) (2016) 15010. https://doi.org/10.1038/natrevmats.2015.10.

[4] W. Yang, R.R. Prabhakar, J. Tan, S.D. Tilley, J. Moon, Strategies for enhancing the

photocurrent, photovoltage, and stability of photoelectrodes for photoelectrochemical water splitting, Chem. Soc. Rev. 48(19) (2019) 4979-5015. https://doi.org/10.1039/c8cs00997j.

[5] Y. Yu, Z. Zhang, X. Yin, A. Kvit, Q. Liao, Z. Kang, X. Yan, Y. Zhang, X. Wang, Enhanced photoelectrochemical efficiency and stability using a conformal TiO_2 film on a black silicon photoanode, Nat. Energy 2(6) (2017) 17045. https://doi.org/10.1038/nenergy.2017.45.

[6] A. Iwase, A. Kudo, Y. Numata, M. Ikegami, T. Miyasaka, N. Ichikawa, M. Kato, H. Hashimoto, H. Inoue, O. Ishitani, H. Tamiaki, Solar Water Splitting Utilizing a SiC Photocathode, a $BiVO_4$ Photoanode, and a Perovskite Solar Cell, ChemSusChem 10(22) (2017) 4420-4423. https://doi.org/10.1002/cssc.201701663.

[7] C. Li, T. Hisatomi, O. Watanabe, M. Nakabayashi, N. Shibata, K. Domen, J.J. Delaunay, Positive onset potential and stability of Cu_2O-based photocathodes in water splitting by atomic layer deposition of a Ga_2O_3 buffer layer, Energy Environ. Sci. 8(5) (2015) 1493-1500. https://doi.org/10.1039/c5ee00250h.

[8] J. Su, T. Minegishi, M. Katayama, K. Domen, Photoelectrochemical hydrogen evolution from water on a surface modified CdTe thin film electrode under simulated sunlight, J. Mater. Chem. A 5(9) (2017) 4486-4492. https://doi.org/10.1039/c6ta10490h.

[9] K. Feng, D. Huang, L. Li, K. Wang, J. Li, T. Harada, S. Ikeda, F. Jiang, MoS_x-CdS/Cu_2ZnSnS_4-based thin film photocathode for solar hydrogen evolution from water, Appl. Catal. B 268 (2020) 118438. https://doi.org/10.1016/j.apcatb.2019.118438.

[10] Y.F. Tay, H. Kaneko, S.Y. Chiam, S. Lie, Q. Zheng, B. Wu, S.S. Hadke, Z. Su, P.S. Bassi, D. Bishop, T.C. Sum, T. Minegishi, J. Barber, K. Domen, L.H. Wong, Solution-Processed Cd-Substituted CZTS Photocathode for Efficient Solar Hydrogen Evolution from Neutral Water, Joule 2(3) (2018) 537-548. https://doi.org/10.1016/j.joule.2018.01.012.

[11] M.P. Suryawanshi, U.V. Ghorpade, S.W. Shin, M.G. Gang, X. Wang, H. Park, S.H. Kang, J.H. Kim, Enhanced Solar Water Oxidation Performance of TiO_2 via Band Edge Engineering: A Tale of Sulfur Doping and Earth-Abundant CZTS Nanoparticles Sensitization, ACS Catal. 7(12) (2017) 8077-8089. https://doi.org/10.1021/acscatal.7b02102.

[12] N. Guijarro, M.S. Prévot, X. Yu, X.A. Jeanbourquin, P. Bornoz, W. Bourée, M. Johnson, F. Le Formal, K. Sivula, A Bottom-Up Approach toward All-Solution-

Processed High-Efficiency Cu(In,Ga)S_2 Photocathodes for Solar Water Splitting, Adv. Energy Mater. 6(7) (2016) 1501949. https://doi.org/10.1002/aenm.201501949.

[13] R.R. Prabhakar, T. Moehl, S. Siol, J. Suh, S.D. Tilley, Sb_2S_3/TiO_2 Heterojunction Photocathodes: Band Alignment and Water Splitting Properties, Chem. Mater. 32(17) (2020) 7247-7253. https://doi.org/10.1021/acs.chemmater.0c01581.

[14] J. Tan, W. Yang, H. Lee, J. Park, K. Kim, O.S. Hutter, L.J. Phillips, S. Shim, J. Yun, Y. Park, J. Lee, J.D. Major, J. Moon, Surface restoration of polycrystalline Sb_2Se_3 thin films by conjugated molecules enabling high-performance photocathodes for photoelectrochemical water splitting, Appl. Catal. B 286 (2021) 119890. https://doi.org/10.1016/j.apcatb.2021.119890.

[15] S. Zhang, M. Long, P. Zhang, J. Wang, H. Lu, H. Xie, A. Tang, H. Yang, Crystallographic orientation and morphology control of Sb_2Se_3 to sensitize TiO_2 nanotube arrays for enhanced photoelectrochemical performances, Chem. Eng. J. 429 (2022) 132091. https://doi.org/10.1016/j.cej.2021.132091.

[16] Y. Zhou, L. Wang, S. Chen, S. Qin, X. Liu, J. Chen, D.J. Xue, M. Luo, Y. Cao, Y. Cheng, E.H. Sargent, J. Tang, Thin-film Sb_2Se_3 photovoltaics with oriented one-dimensional ribbons and benign grain boundaries, Nat. Photonics 9(6) (2015) 409-415. https://doi.org/10.1038/nphoton.2015.78.

[17] S. Chen, T. Liu, Z. Zheng, M. Ishaq, G. Liang, P. Fan, T. Chen, J. Tang, Recent progress and perspectives on Sb_2Se_3-based photocathodes for solar hydrogen production via photoelectrochemical water splitting, J. Energy Chem. (2021). https://doi.org/10.1016/j.jechem.2021.08.062.

[18] H. Zhou, M. Feng, K. Song, B. Liao, Y. Wang, R. Liu, X. Gong, D. Zhang, L. Cao, S. Chen, A highly [001]-textured Sb_2Se_3 photocathode for efficient photoelectrochemical water reduction, Nanoscale 11(47) (2019) 22871-22879. https://doi.org/10.1039/c9nr08700a.

[19] Q. Cai, W. Hong, C. Jian, W. Liu, A high-performance silicon photoanode enabled by oxygen vacancy modulation on NiOOH electrocatalyst for water oxidation, Nanoscale 12(14) (2020) 7550-7556. https://doi.org/10.1039/d0nr00921k.

[20] H. Kaneko, T. Minegishi, M. Nakabayashi, N. Shibata, Y. Kuang, T. Yamada, K. Domen, A Novel Photocathode Material for Sunlight-Driven Overall Water Splitting: Solid Solution of ZnSe and Cu(In,Ga)Se_2, Adv. Funct. Mater. 26(25) (2016) 4570-4577. https://doi.org/10.1002/adfm.201600615.

[21] R.R. Prabhakar, W. Septina, S. Siol, T. Moehl, R. Wick-Joliat, S.D. Tilley,

Photocorrosion-resistant Sb_2Se_3 photocathodes with earth abundant MoS_x hydrogen evolution catalyst, J. Mater. Chem. A 5(44) (2017) 23139-23145. https://doi.org/10.1039/c7ta08993g.

[22] C. Chen, D.C. Bobela, Y. Yang, S. Lu, K. Zeng, C. Ge, B. Yang, L. Gao, Y. Zhao, M.C. Beard, J. Tang, Characterization of basic physical properties of Sb_2Se_3 and its relevance for photovoltaics, Front. Optoelectron. 10(1) (2017) 18-30. https://doi.org/10.1007/s12200-017-0702-z.

[23] J. Kim, W. Yang, Y. Oh, H. Lee, S. Lee, H. Shin, J. Kim, J. Moon, Self-oriented Sb_2Se_3 nanoneedle photocathodes for water splitting obtained by a simple spin-coating method, J. Mater. Chem. A 5 (2017) 2180–2187. https://doi.org/10.1039/C6TA09602F.

[24] W. Yang, J. Ahn, Y. Oh, J. Tan, H. Lee, J. Park, H.C. Kwon, J. Kim, W. Jo, J. Kim, J. Moon, Adjusting the Anisotropy of 1D Sb_2Se_3 Nanostructures for Highly Efficient Photoelectrochemical Water Splitting, Adv. Energy Mater. 8(14) (2018) 1702888. https://doi.org/10.1002/aenm.201702888.

[25] J. Park, W. Yang, J. Tan, H. Lee, J.W. Yun, S.G. Shim, Y.S. Park, J. Moon, Hierarchal Nanorod-Derived Bilayer Strategy to Enhance the Photocurrent Density of Sb_2Se_3 Photocathodes for Photoelectrochemical Water Splitting, ACS Energy Lett. 5(1) (2019) 136-145. https://doi.org/10.1021/acsenergylett.9b02486.

[26] J. Park, W. Yang, Y. Oh, J. Tan, H. Lee, R. Boppella, J. Moon, Efficient Solar-to-Hydrogen Conversion from Neutral Electrolytes using Morphology-Controlled Sb_2Se_3 Light Absorbers, ACS Energy Lett. 4(2) (2019) 517-526. https://doi.org/10.1021/acsenergylett.8b02323.

[27] W. Yang, J.H. Kim, O.S. Hutter, L.J. Phillips, J. Tan, J. Park, H. Lee, J.D. Major, J.S. Lee, J. Moon, Benchmark performance of low-cost Sb_2Se_3 photocathodes for unassisted solar overall water splitting, Nat. Commun. 11(1) (2020) 861. https://doi.org/10.1038/s41467-020-14704-3.

[28] L. Zhang, Y. Li, C. Li, Q. Chen, Z. Zhen, X. Jiang, M. Zhong, F. Zhang, H. Zhu, Scalable Low-Band-Gap Sb_2Se_3 Thin-Film Photocathodes for Efficient Visible-Near-Infrared Solar Hydrogen Evolution, ACS Nano 11(12) (2017) 12753-12763. https://doi.org/10.1021/acsnano.7b07512.

[29] J. Tan, W. Yang, Y. Oh, H. Lee, J. Park, J. Moon, Controlled Electrodeposition of Photoelectrochemically Active Amorphous MoS_x Cocatalyst on Sb_2Se_3 Photocathode, ACS Appl. Mater. Interfaces 10(13) (2018) 10898-10908. https://doi.org/10.1021/acsami.8b00305.

[30] H. Lee, W. Yang, J. Tan, Y. Oh, J. Park, J. Moon, Cu-Doped NiO_x as an Effective Hole-Selective Layer for a High-Performance Sb_2Se_3 Photocathode for Photoelectrochemical Water Splitting, ACS Energy Lett. 4(5) (2019) 995-1003. https://doi.org/10.1021/acsenergylett.9b00414.

[31] J. Tan, W. Yang, Y. Oh, H. Lee, J. Park, R. Boppella, J. Kim, J. Moon, Fullerene as a Photoelectron Transfer Promoter Enabling Stable TiO_2-Protected Sb_2Se_3 Photocathodes for Photoelectrochemical Water Splitting, Adv. Energy Mater. 9(16) (2019) 1900179. https://doi.org/10.1002/aenm.201900179.

[32] W. Yang, J. Park, H.C. Kwon, O.S. Hutter, L.J. Phillips, J. Tan, H. Lee, J. Lee, S.D. Tilley, J.D. Major, J. Moon, Solar water splitting exceeding 10% efficiency via low-cost Sb_2Se_3 photocathodes coupled with semitransparent perovskite photovoltaics, Energy Environ. Sci. 13(11) (2020) 4362-4370. https://doi.org/10.1039/d0ee02959a.

[33] L.L. K. Gelderman, S. W. Donne, Flat-Band Potential of a Semiconductor Using the Mott–Schottky Equation, J. Chem. Educ. 84 (2007) 685-688. https://doi:10.1021/ed084p685

[34] K. Zeng, D.J. Xue, J. Tang, Antimony selenide thin-film solar cells, Semiconductor Sci. Technol. 31(6) (2016) 063001. https://doi.org/10.1088/0268-1242/31/6/063001.

[35] R. Beranek, Photoelectrochemical Methods for the Determination of the Band Edge Positions of TiO_2-Based Nanomaterials, Adv. Phys. Chem. 2011 (2011) 1-20. https://doi.org/10.1155/2011/786759.

[36] G.X. Liang, Z.H. Zheng, P. Fan, J.T. Luo, J.G. Hu, X.H. Zhang, H.L. Ma, B. Fan, Z.K. Luo, D.P. Zhang, Thermally induced structural evolution and performance of Sb_2Se_3 films and nanorods prepared by an easy sputtering method, Sol. Energy Mater. Sol. Cells 174 (2018) 263-270. https://doi.org/10.1016/j.solmat.2017.09.008.

[37] P. Vidal-Fuentes, M. Guc, X. Alcobe, T. Jawhari, V. Izquierdo-Roca, Multiwavelength excitation Raman scattering study of Sb_2Se_3 compound: fundamental vibrational properties and secondary phases detection, 2D Mater. 6 (2019) 045054. https://doi.org/10.1088/2053-1583/ab4029.

[38] G.P. Saxena, R. Mangal, A. Mishra, T.P. Sharma, Band gap determination of Ni–Zn ferrites, Bull. Mater. Sci. 26(4) (2003) 387-389. https://doi:10.1007/bf02711181.

[39] G. Liang, X. Chen, R. Tang, Y. Liu, Y. Li, P. Luo, Z. Su, X. Zhang, P. Fan, S. Chen, Spark plasma sintering of Sb_2Se_3 sputtering target towards highly efficient thin film solar cells, Sol. Energy Mater. Sol. Cells 211 (2020) 110530.

https://doi.org/10.1016/j.solmat.2020.110530.

[40] K. Zhang, M. Ma, P. Li, D.H. Wang, J.H. Park, Water Splitting Progress in Tandem Devices: Moving Photolysis beyond Electrolysis, Adv. Energy Mater. 6(15) (2016) 1600602. https://doi.org/10.1002/aenm.201600602.

[41] H. Zhou, M. Feng, M. Feng, X. Gong, D. Zhang, Y. Zhou, S. Chen, Gradient doping of sulfur in Sb_2Se_3 nanowire arrays as photoelectrochemical photocathode with a 2% half-cell solar-to-hydrogen conversion efficiency, Appl. Phys. Lett. 116(11) (2020) 113902. https://doi.org/10.1063/1.5142582.

[42] C. Liu, T. Liu, Y. Li, Z. Zhao, D. Zhou, W. Li, Y. Zhao, H. Yang, L. Sun, F. Li, Z. Li, A dendritic Sb_2Se_3/In_2S_3 heterojunction nanorod array photocathode decorated with a MoS_x catalyst for efficient solar hydrogen evolution, J. Mater. Chem. A 8(44) (2020) 23385-23394. https://doi.org/10.1039/d0ta08874a.

[43] B. Weng, M.Y. Qi, C. Han, Z.R. Tang, Y.J. Xu, Photocorrosion Inhibition of Semiconductor-Based Photocatalysts: Basic Principle, Current Development, and Future Perspective, ACS Catal. 9(5) (2019) 4642-4687. https://doi.org/10.1021/acscatal.9b00313.

[44] G.X. Liang, Y.D. Luo, S. Chen, R. Tang, Z.H. Zheng, X.J. Li, X.S. Liu, Y.K. Liu, Y.F. Li, X.Y. Chen, Z.H. Su, X.H. Zhang, H.L. Ma, P. Fan, Sputtered and selenized Sb_2Se_3 thin-film solar cells with open-circuit voltage exceeding 500 mV, Nano Energy 73 (2020) 104806. https://doi.org/10.1016/j.nanoen.2020.104806.

[45] M.B. Costa, F.W.S. Lucas, M. Medina, L.H. Mascaro, All-Electrochemically Grown Sb_2Se_3/a-MoS_x Photocathodes for Hydrogen Production: The Effect of the MoS_x Layer on the Surface Recombination and Photocorrosion of Sb_2Se_3 Films, ACS Appl. Energy Mater. 3(10) (2020) 9799-9808. https://doi.org/10.1021/acsaem.0c01413.

[46] X. Chen, Z. Li, H. Zhu, Y. Wang, B. Liang, J. Chen, Y. Xu, Y. Mai, CdS/Sb_2S_3 heterojunction thin film solar cells with a thermally evaporated absorber, J. Mater. Chem. C 5(36) (2017) 9421-9428. https://doi.org/10.1039/c7tc02460f.

[47] K. Sun, C. Yan, F. Liu, J. Huang, F. Zhou, J.A. Stride, M. Green, X. Hao, Over 9% Efficient Kesterite Cu_2ZnSnS_4 Solar Cell Fabricated by Using $Zn_{1-x}Cd_xS$ Buffer Layer, Adv. Energy Mater. 6(12) (2016) 1600046. https://doi.org/10.1002/aenm.201600046.

[48] Z. Su, G. Liang, P. Fan, J. Luo, Z. Zheng, Z. Xie, W. Wang, S. Chen, J. Hu, Y. Wei, C. Yan, J. Huang, X. Hao, F. Liu, Device Postannealing Enabling over 12% Efficient Solution-Processed Cu_2 $ZnSnS_4$ Solar Cells with Cd^{2+} Substitution, Adv. Mater. 32(32) (2020) e2000121. https://doi.org/10.1002/adma.202000121.

[49] D. Klotz, D.A. Grave, A. Rothschild, Accurate determination of the charge transfer efficiency of photoanodes for solar water splitting, Phys. Chem. Chem. Phys. 19(31) (2017) 20383-20392. https://doi.org/10.1039/c7cp02419c.

[50] T. Zhou, S. Chen, J. Wang, Y. Zhang, J. Li, J. Bai, B. Zhou, Dramatically enhanced solar-driven water splitting of $BiVO_4$ photoanode via strengthening hole transfer and light harvesting by co-modification of CQDs and ultrathin β-FeOOH layers, Chem. Eng. J. 403 (2021) 126350. https://doi.org/10.1016/j.cej.2020.126350.

[51] Y. Li, K. Wang, D. Huang, L. Li, J. Tao, N.A.A. Ghany, F. Jiang, $CdxZn_{1-x}S/Sb_2Se_3$ thin film photocathode for efficient solar water splitting, Appl. Catal. B 286 (2021) 119872. https://doi.org/10.1016/j.apcatb.2020.119872.

[52] Y.D. Luo, R. Tang, S. Chen, J.G. Hu, Y.K. Liu, Y.F. Li, X.S. Liu, Z.H. Zheng, Z.H. Su, X.F. Ma, P. Fan, X.H. Zhang, H.L. Ma, Z.G. Chen, G.X. Liang, An effective combination reaction involved with sputtered and selenized Sb precursors for efficient Sb_2Se_3 thin film solar cells, Chem. Eng. J. 393 (2020) 124599. https://doi.org/10.1016/j.cej.2020.124599.

[53] C. Yan, J. Huang, K. Sun, S. Johnston, Y. Zhang, H. Sun, A. Pu, M. He, F. Liu, K. Eder, L. Yang, J.M. Cairney, N.J. Ekins-Daukes, Z. Hameiri, J.A. Stride, S. Chen, M.A. Green, X. Hao, Cu_2ZnSnS_4 solar cells with over 10% power conversion efficiency enabled by heterojunction heat treatment, Nat. Energy 3(9) (2018) 764-772. https://doi.org/10.1038/s41560-018-0206-0.

[54] X. Zhang, F. Shi, J. Niu, Y. Jiang, Z. Wang, Superhydrophobic surfaces: from structural control to functional application, J. Mater. Chem. 18(6) (2008) 621-633. https://doi.org/10.1039/b711226b.

[55] F. Foadi, G.H. ten Brink, M.R. Mohammadizadeh, G. Palasantzas, Roughness dependent wettability of sputtered copper thin films: The effect of the local surface slope, J. Appl. Phys. 125(24) (2019) 244307. https://doi.org/10.1063/1.5092672.

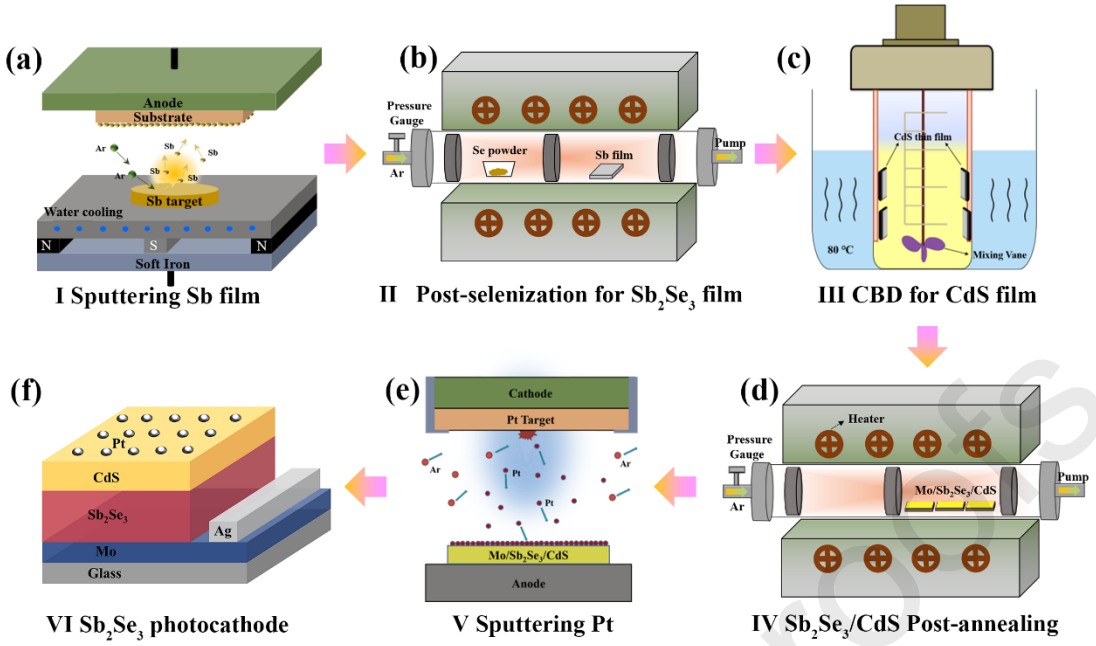

Fig. 1. Schematic illustration of the preparation process of the Sb_2Se_3 thin film photocathode. (a) Sb precursor thin film deposited by RF magnetron sputtering, (b) Sb_2Se_3 thin film obtained by post-selenization heat treatment, (c) CdS buffer layer obtained by CBD method, (d) Post-annealing of the Sb_2Se_3/CdS heterojunction, (e) Pt co-catalyst deposited by sputtering, (f) Schematic configuration of the as-prepared Sb_2Se_3 thin film photocathode.

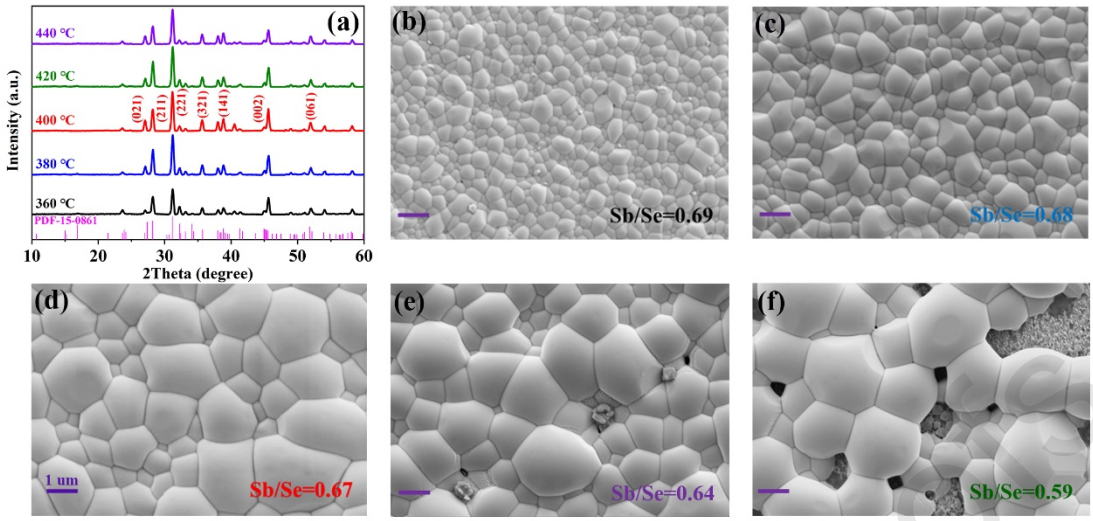

Fig. 2. (a) XRD patterns, and (b-f) top-view SEM images of the Sb_2Se_3 thin films prepared at different selenization temperatures of 360 °C, 380 °C, 400 °C, 420 °C, and 440 °C, respectively.

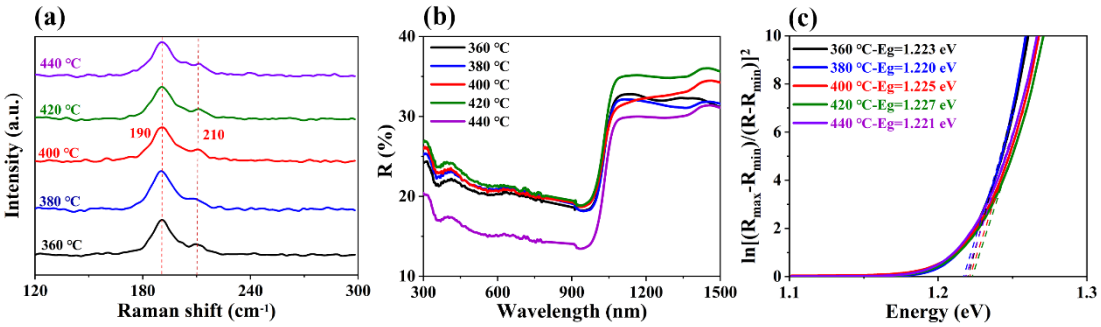

Fig. 3. Optical characterizations of the Sb_2Se_3 thin films selenized at different temperatures. (a) Raman spectra, (b) Reflection spectra, (c) Plot of $\ln[(R_{max}-R_{min})/(R-R_{min})]^2$ versus Energy, used to obtain direct bandgap.

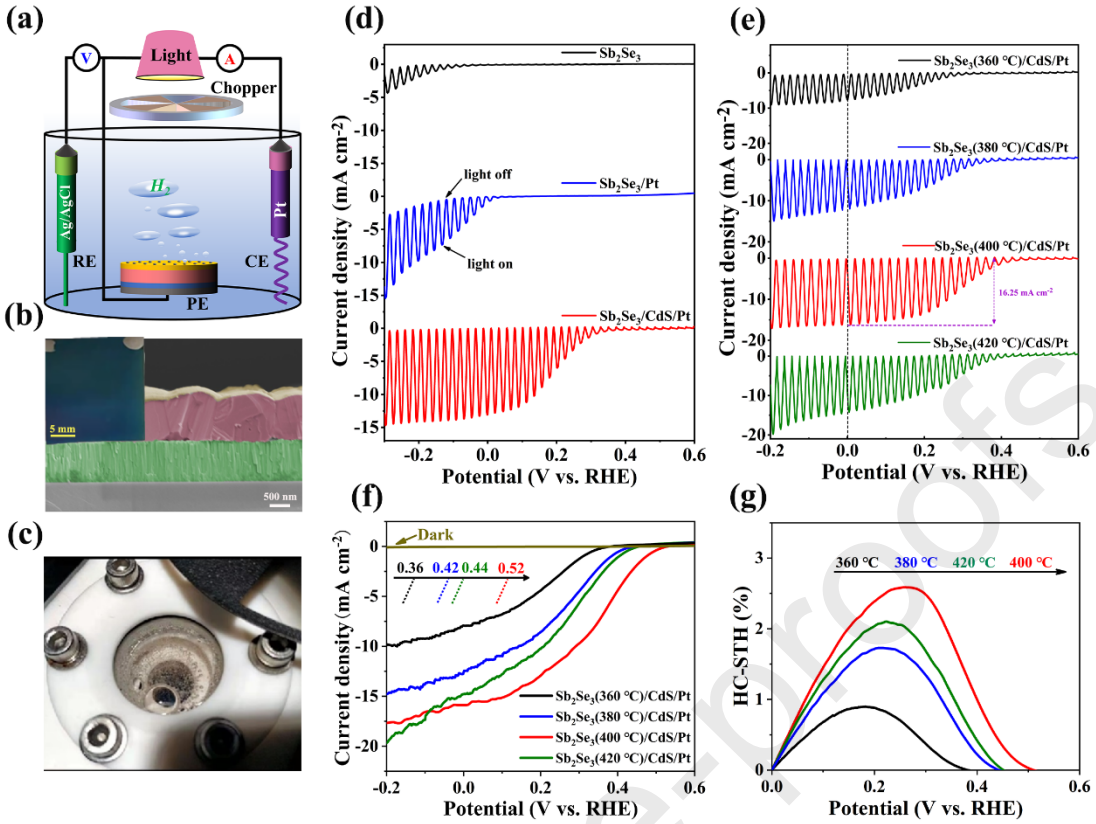

Fig. 4. (a) Schematic diagram of the 3-electrode PEC measurement. (b) Cross-sectional SEM image of the representative Mo/Sb_2Se_3/CdS/Pt thin film photocathode, and a photograph of the entire photocathode (inset). (c) An experimental observed photograph with hydrogen bubbles emerged from photocathode surface to the electrolyte under illumination. (d) *J-V* curves of bare Sb_2Se_3, Sb_2Se_3/Pt, and Sb_2Se_3/CdS/Pt photocathodes under chopped illumination of AM 1.5G simulated sunlight. (e) Chopped light illumination, and (f) dark and continuous light illumination determined *J-V* curves of the Sb_2Se_3/CdS/Pt photocathodes with Sb_2Se_3 thin films selenized at different temperatures, enlarged view of the onset potential are also inset in (f). (g) The corresponding HC-STH conversion efficiencies.

Table 1. Summary of the PEC performance for some recently reported Sb_2Se_3 photocathodes

Photocathode	Electrolyte	J_{ph} (mA cm^{-2} at 0 V_{RHE})	V_{on} (V_{RHE})	HC-STH (%)	Ref.
SLG/Mo/Sb_2Se_3/CdS/Pt	**0.5M H_2SO_4**	**16.25**	**0.52**	**2.58%**	**This work**
SLG/Mo/Sb_2Se_3/CdS/TiO_2/Pt	0.5M $NaSO_4$	8.6	0.43	N/A	[28]
SLG/Mo/Sb_2Se_3/TiO_2/Pt	1M H_2SO_4	20.2	0.30	1.36%	[18]
SLG/Mo/grad-S:Sb_2Se_3/TiO_2/Pt	1M H_2SO_4	14.2	0.42	2%	[41]
SLG/Mo/Sb_2Se_3/In_2S_3/MoS_x	0.1M H_2SO_4	27	0.40	2.6%	[42]
FTO/Au/Sb_2Se_3/TiO_2/Pt	0.1M H_2SO_4	12.5	0.35	N/A	[24]
FTO/Au/Sb_2Se_3/CdS/TiO_2/Pt	0.1M H_2SO_4	13.5	0.47	N/A	[26]
FTO/Au/Sb_2Se_3/CdS/TiO_2/Pt	pH 1 H_2SO_4	19	0.50	3.4%	[27]

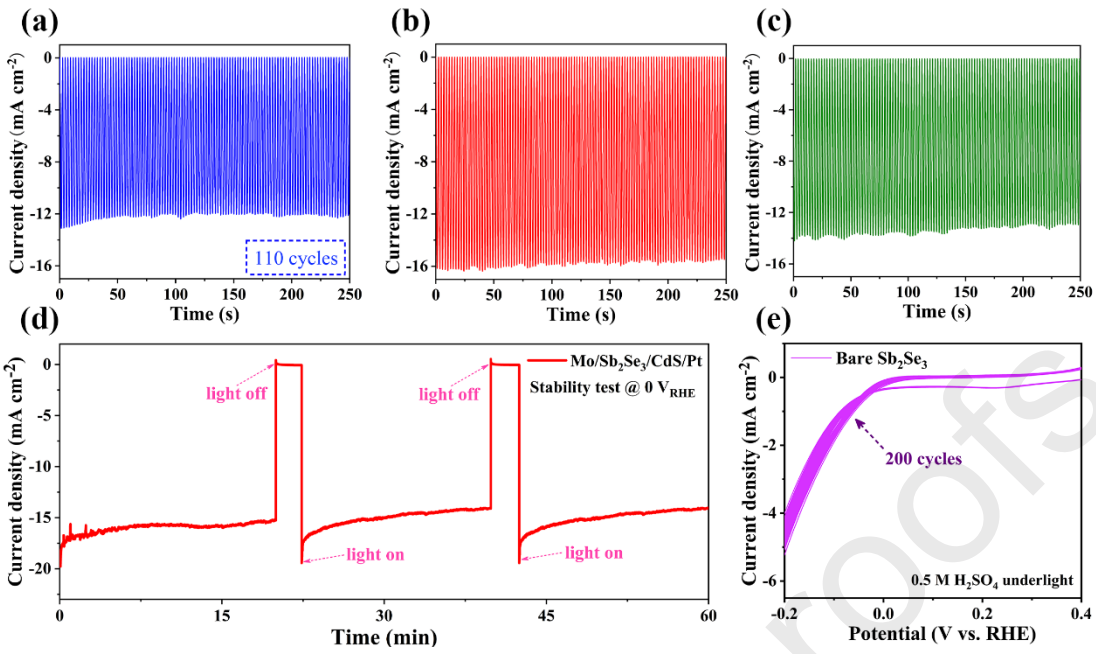

Fig. 5. (a-c) *J-T* curves of the Sb_2Se_3/CdS/Pt photocathodes at 0 V_{RHE} under AM 1.5G simulated sunlight illumination, wherein the Sb_2Se_3 thin films were selenized at 380 °C, 400 °C and 420 °C, respectively. (d) Photocurrent stability test of the champion Sb_2Se_3 photocathode at 0 V_{RHE} under illumination within 60 min. (e) Cyclic voltammetry measurement of a bare Sb_2Se_3 thin film in 0.5 M H_2SO_4 under illumination.

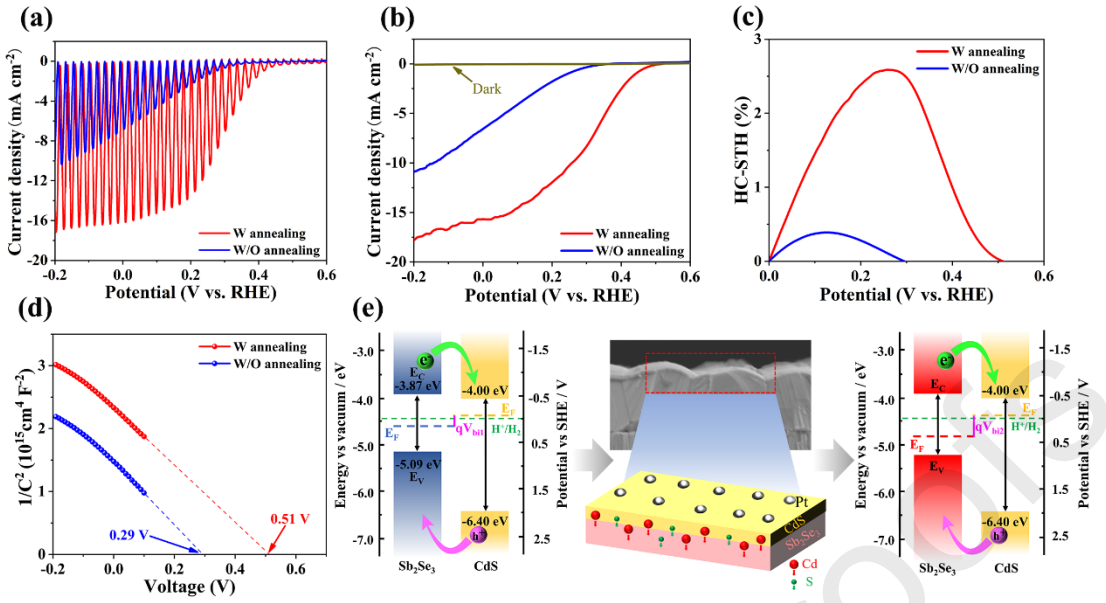

Fig. 6. (a-b) *J-V* curves of the Mo/Sb_2Se_3/CdS/Pt photocathodes with (W) or without (W/O) post-annealing of the Sb_2Se_3/CdS heterojunction, and under chopped light and continuous light illumination, respectively. (c) The corresponding HC-STH conversion efficiencies. (d) $1/C^2$-*V* plots of the photocathodes. (e) Schematic illustration of energy-level alignment of the Sb_2Se_3/CdS (W/O) (left), Sb_2Se_3/CdS (W) (right), and a diagram of the post-annealing induced elemental inter-diffusion of Cd and S (middle).

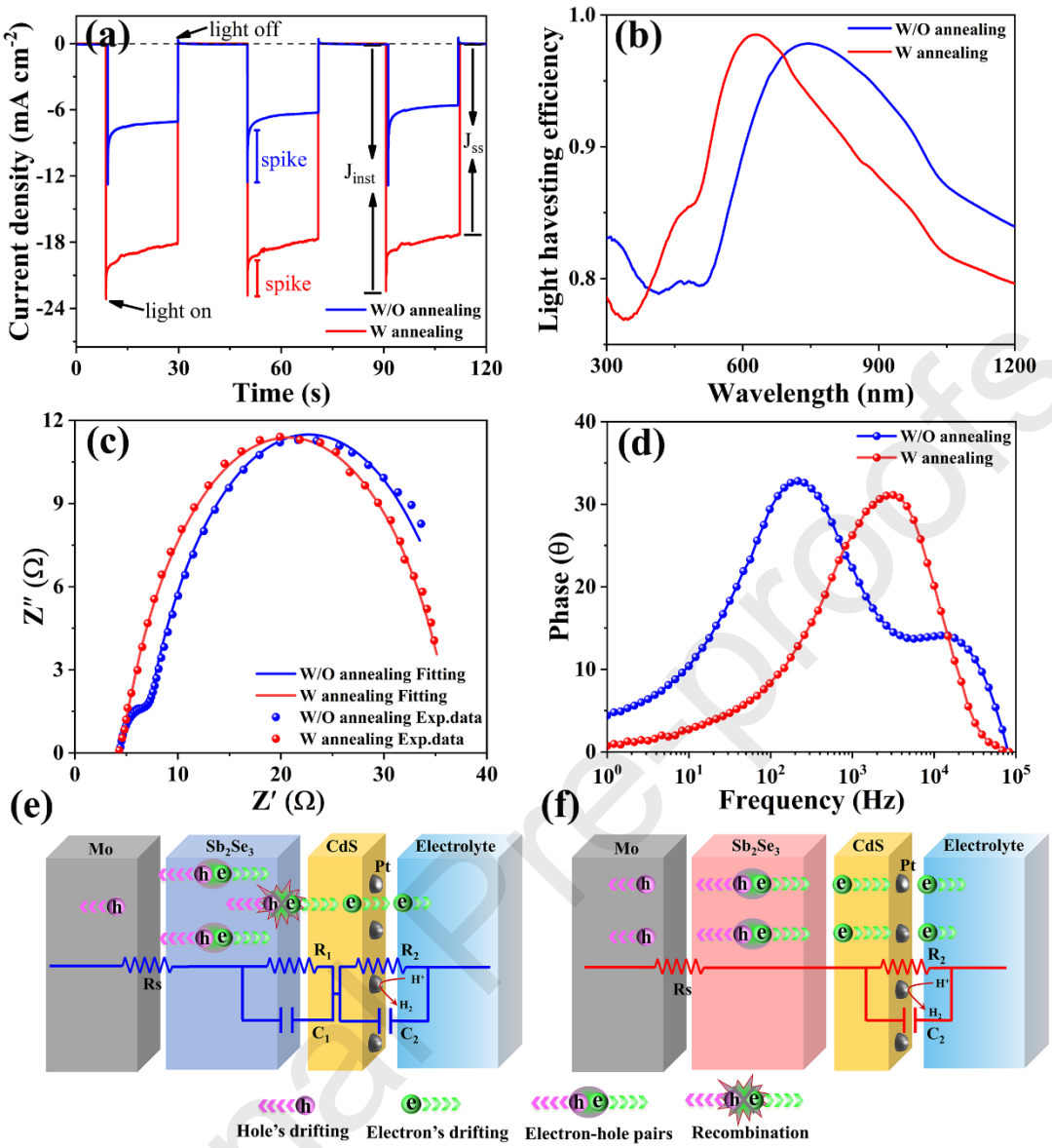

Fig. 7. (a) Transient photocurrent response, and (b) Light harvesting efficiency (*LHE*) of the Mo/Sb_2Se_3/CdS/Pt photocathodes with (W) or without (W/O) Sb_2Se_3/CdS heterojunction post-annealing. PEIS characterizations of the photocathodes: (c) Nyquist plots, and (d) Bode plots. Equivalent circuit diagrams and schematic illustrations of the charge transfer processes associated to (e) the non-annealed device, and (f) the annealed counterpart.

Table 2. Summary the values associated to charge transport kinetics parameters

Device Structure	η_{tran}	η_{sep}	R_s (Ω)	R_1 (Ω)	C_1 (μF)	R_2 (Ω)	C_2 (μF)
Mo/Sb_2Se_3/CdS (W/O)/Pt	34%	49%	4.6	2.03	1.89	32.1	280
Mo/Sb_2Se_3/CdS (W)/Pt	70%	63%	4.6	/	/	26.7	4.57

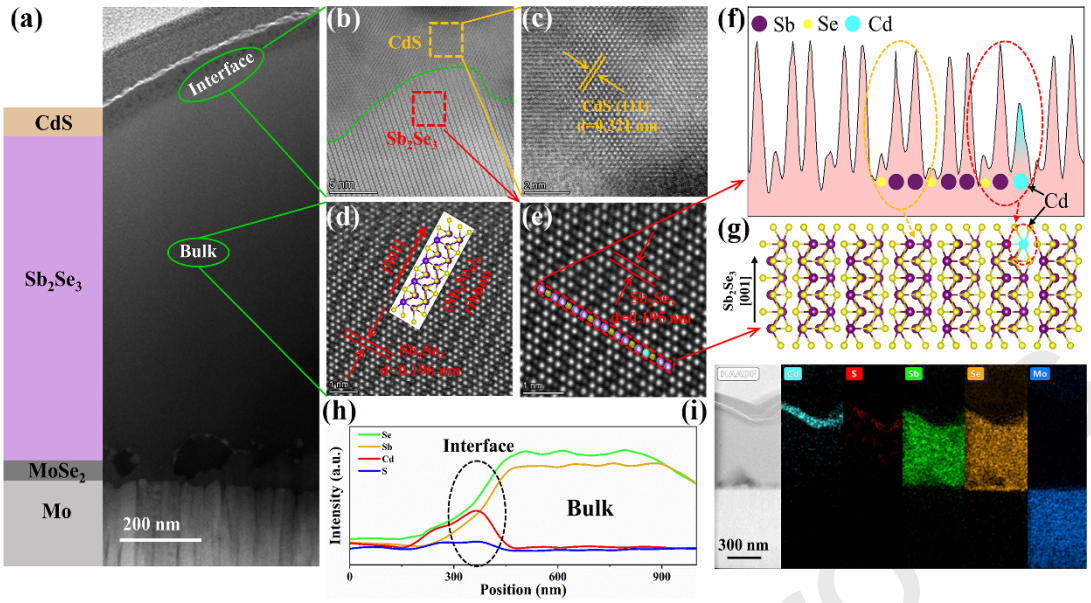

Fig. 8. TEM characterizations of the annealed Mo/Sb_2Se_3/CdS (W)/Pt photocathode. (a) Cross-sectional TEM image of the device, (b) HRTEM image of the Sb_2Se_3/CdS heterojunction interface, (c) HRTEM analysis of the selected CdS buffer layer region. (d) and (e) represent the HAADF-STEM images (with Gaussian blur processed) of Sb_2Se_3 taken inside the bulk absorber layer region and near the interface region, respectively. (f) The intensity profiles of the HAADF signals from the marked red rectangular frame. (g) Atomic configuration of Sb_2Se_3 with $(Sb_4Se_6)_n$ ribbons stacked in parallel in the [001] direction. (h) EDS elemental line scan profiles across Sb_2Se_3 bulk region and Sb_2Se_3/CdS interface region. (i) The corresponding EDS elemental mappings of Cd, S, Sb, Se, and Mo, used to reveal the compositional distribution.

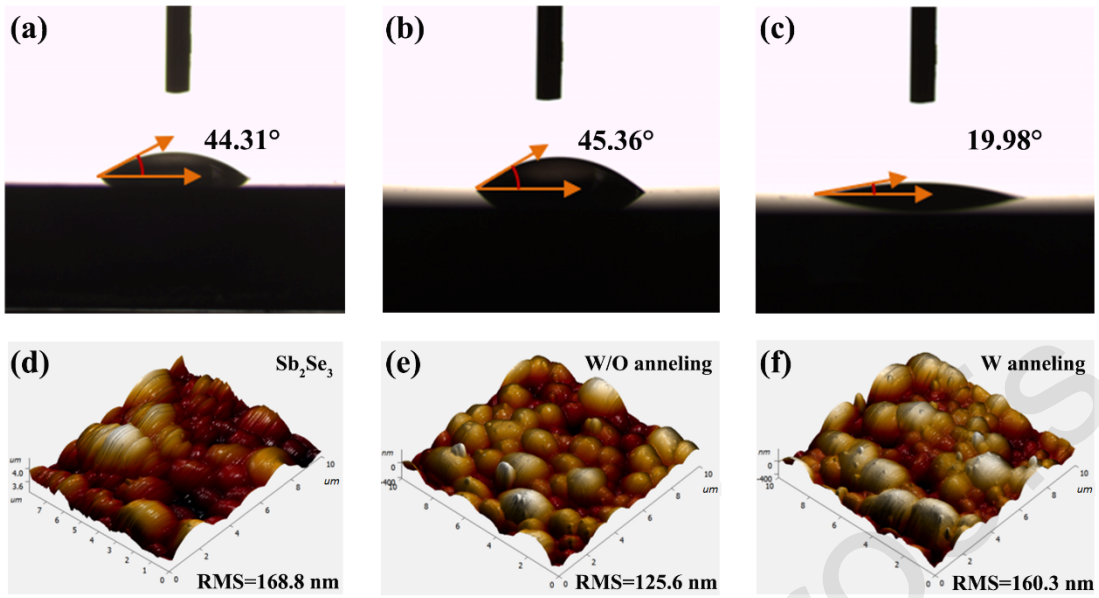

Fig. 9. (a-c) The measured *CAs* of pure Sb_2Se_3, Sb_2Se_3/CdS (W/O annealing), and Sb_2Se_3/CdS (W annealing) films, respectively. (d-f) The corresponding AFM topographical images.

Graphical Abstract

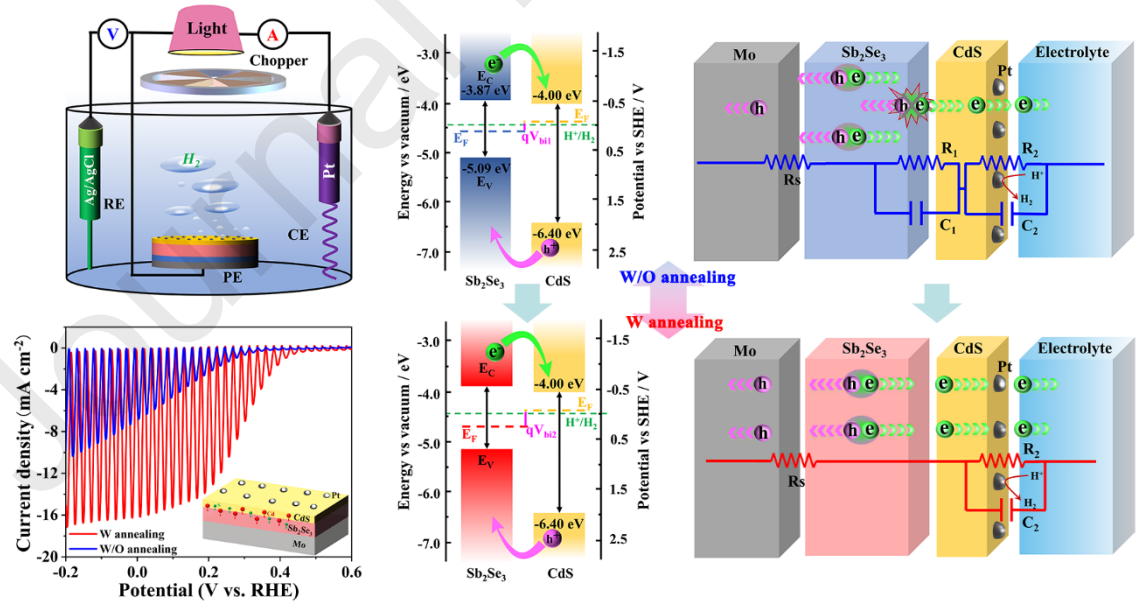

Mo/Sb_2Se_3/CdS/Pt photocathode was constructed for PEC processed solar hydrogen production. Interestingly, an efficient interface engineering of Sb_2Se_3/CdS heterojunction post-annealing strongly improved device performance through modifying energy-level alignment, reducing interfacial recombination loss, and strengthening charge transport.

Highlights

- Self-assembled growth of high-quality Sb_2Se_3 via sputtered and selenized Sb precursor
- Mo/Sb_2Se_3/CdS/Pt photocathode delivers J_{ph} of 16.25 mA cm^{-2}, V_{on} of 0.52 V_{RHE}
- An interface engineering of heterojunction post-annealing plays an important role
- It can modify band alignment, reduce recombination, improve charge transfer, and wettability
- Enhancing overall PEC performance with HC-STH conversion efficiency of 2.58%